Dynamics of electrohydraulic soft actuators

Philipp Rothemund[a,1], Sophie Kirkman[a], and Christoph Keplinger[a,b,1]

[a]Department of Mechanical Engineering, University of Colorado, Boulder, CO 80309; and [b]Materials Science and Engineering Program, University of Colorado, Boulder, CO 80303

Edited by John A. Rogers, Northwestern University, Evanston, IL, and approved May 31, 2020 (received for review April 7, 2020)

Nature has inspired the design of robots in which soft actuators enable tasks such as handling of fragile objects and adapting to unstructured environments. Those tasks are difficult for traditional robots, which predominantly consist of hard components. Electrohydraulic soft actuators are liquid-filled shells that deform upon the application of electric fields; they excel among soft actuators with muscle-like force outputs and actuation strains, and with actuation frequencies above 100 Hz. However, the fundamental physics that governs the dynamics of electrohydraulic soft actuators is unexplored. Here, we study the dynamics of electrohydraulic soft actuators using the Peano-HASEL (hydraulically amplified self-healing electrostatic) actuator as a model system. Using experiments and a scaling analysis, we discover two dynamic regimes: a regime in which viscous dissipation reduces the actuation speed and a regime governed by inertial effects in which high-speed actuation is possible. For each regime, we derive a timescale that describes the influence of geometry, materials system, and applied external loads on the actuation speed. We also derive a model to study the dynamic behavior of Peano-HASEL actuators in both regimes. Although this analysis focuses on the Peano-HASEL actuator, the presented results may readily be generalized to other electrohydraulic actuators. When designed to operate in the inertial regime, electrohydraulic actuators will enable bio-inspired robots with unprecedented speeds of motion.

soft robotics | electrohydraulic actuator | dynamics | modeling | scaling analysis

Organisms in nature make use of soft tissue, such as muscle and skin, to change shape and to adapt to new tasks and environments (1). Traditionally, human-built machines predominantly rely on hard materials and components, such as metals and gears, and outperform natural organisms in force and precision. However, these hard machines often struggle in unstructured environments that require adaptability. Therefore, the designs found in nature have served as inspiration for the development of machines and robots in which soft materials enable unique functionalities. In particular, soft actuators (2–4) have emerged as key building blocks for robots that can navigate in unstructured environments (5, 6), handle delicate objects (3, 4), and safely interact with humans (7–9). Electrohydraulic soft actuators are composed of deformable, liquid-filled shells that deform under electric fields (4, 10, 11). They have drawn attention as high-performance actuators (4, 11–14), as they achieve large actuation strains (>100%) and stresses (>0.3 MPa), and high specific powers (>600 W/kg) and frequencies (>100 Hz) (12). We (15, 16) and others (17–19) have investigated the quasistatic behavior of electrohydraulic soft actuators, but the fundamental physics that governs their dynamic behavior is unexplored.

Electrohydraulic soft actuators combine the working principles of dielectric elastomer actuators (DEAs) (2) and fluid-driven soft actuators (9), but their dynamic behavior is different from both technologies. Electrohydraulic soft actuators and DEAs both use electrostatic forces for activation (4, 20, 21). However, the dynamics of DEAs is governed by elastic effects (22–27), whereas elasticity only plays a minor role in many designs of electrohydraulic soft actuators (11, 12, 15). A working fluid drives the shape change of both electrohydraulic and fluid-driven soft actuators (4, 9). However, for fluid-driven soft actuators, external pumps regulate the fluid flow (3, 9) and flow resistance of the channels between the pumps and the actuators typically governs their actuation speed (28–30), thereby limiting their actuation frequencies to ∼1 Hz when the working fluid is liquid (29). In contrast, liquid is only redistributed locally in electrohydraulic soft actuators; to date, it is not understood what governs their actuation speed.

Here, we investigate the fundamental physical principles that govern the dynamic behavior of electrohydraulic soft actuators using the Peano-HASEL (hydraulically amplified self-healing electrostatic) actuator as a model system (11). Using scaling laws, we identify a viscous timescale and an inertial timescale that depend on the materials system and geometry of the actuators and the operating conditions. Depending on the ratio of these timescales, regimes with distinctly different dynamic behavior emerge: 1) a regime in which viscous effects govern the actuation speed; 2) a regime in which inertial effects govern the actuation speed. We experimentally confirm the existence of these regimes over a range of parameters that span multiple orders of magnitude. We also derive a model to calculate the actuation speed of Peano-HASEL actuators in the entire experimentally investigated range of parameters and to investigate

Significance

Soft actuators have opened avenues for the design of robots that excel in unstructured environments. Electrohydraulic soft actuators are liquid-filled shells that deform due to electrostatic forces. This working principle enables large design freedom and actuator performance that rivals natural muscle. However, the fundamental physics that governs the dynamics of electrohydraulic soft actuators is virtually unexplored. Here, we show how scale, geometry, and materials system of the actuators, as well as external applied loads and voltages lead to actuation speeds that span multiple orders of magnitude. The presented principles and conclusions can readily be applied to analyze the dynamic behavior of various types of electrohydraulic actuators and to provide guidelines on how to increase actuation speed in bio-inspired robotic systems.

Author contributions: P.R. and C.K. designed research; P.R. and S.K. performed research; P.R. and S.K. analyzed data; P.R., S.K., and C.K. wrote the paper; and C.K. supervised the research.

Competing interest statement: C.K. is a co-founder of Artimus Robotics, a startup company commercializing HASEL actuators. C.K. is listed as inventor on PCT applications PCT/US18/023797 and PCT/US19/020568 that cover fundamentals and basic designs of HASEL actuators.

This article is a PNAS Direct Submission.

Data deposition: All of the data reported in this paper as well as the Matlab code to calculate the transition times have been deposited to Figshare, https://dx.doi.org/10.6084/m9.figshare.c.4965041.v1.

[1]To whom correspondence may be addressed. Email: philipp.rothemund@colorado.edu or christoph.keplinger@colorado.edu.

This article contains supporting information online at https://www.pnas.org/lookup/suppl/doi:10.1073/pnas.2006596117/-/DCSupplemental.

First published June 29, 2020.

the influence of applied voltages and loads. Even though the analysis is focused on the Peano-HASEL actuator, the presented results and principles can readily be applied to other electrohydraulically activated soft systems.

Results

Experimental Design. A HASEL actuator consists of a flexible polymer shell that is coated with flexible electrodes and filled with a liquid dielectric (Fig. 1*A*). When connected to a voltage supply, charges flow onto the electrodes. The electrostatic attraction between the electrodes causes "zipping" of the shell, thereby displacing the liquid dielectric against viscous resistance. The actuator deforms and lifts a weight. When the voltage is turned off, the weight exerts a force on the actuator that causes the electrodes to unzip and the liquid dielectric to flow back between the electrodes (Fig. 1*B*). The Peano-HASEL actuator (11) (Fig. 1*C*) is a specific design of HASEL actuator in which two inextensible but flexible polymer films are bonded to form a rectangular shell. The top half of the shell is covered on both sides over the entire width with flexible electrodes. Rigid frames on the top and bottom of the actuator are used for load introduction. When a voltage is applied to the actuator, the electrodes zip together from the top of the actuator, and the actuator contracts in length (Fig. 1*D*). We use the Peano-HASEL actuator as a model system for electrohydraulic soft actuators, as its rectangular geometry simplifies modeling and interpretation of experimental results.

To study the dynamic behavior of Peano-HASEL actuators, we suspended them from the top frame and attached weights of mass M to the bottom frame (Fig. 2*A*; see *Materials and Methods* for details of experimental setup). We applied square wave voltage signals of voltage Φ to the actuators and measured their deformation as a function of time by tracking a marker on the bottom frame with a high-speed camera. In our experiments, we not only varied M and Φ, but we also used actuators with shells of different length L and width w, shell materials of different thickness h and relative permittivity ε_r, and liquid dielectrics of different viscosity μ (Fig. 2 *A* and *B*; see *Materials and Methods* for details of fabrication and materials). Varying these parameters changed the time in which the actuators contracted (Fig. 2*C*) and elongated (Fig. 2*E*). To capture the entire process of contraction and elongation, we adjusted the frequency of the voltage signal so that all actuators could contract to a zipped equilibrium (Fig. 2*D*) when the voltage turned on, and fully relax (Fig. 2*B*) when the voltage turned off. To compare the recorded data from actuators of different lengths, we calculated the actuation strain $e = x/l_0$, where x is the measured stroke, and l_0 is the unzipped length of the actuators (Fig. 2 *B* and *C*).

Depending on geometry and materials system, we observed two qualitatively different types of dynamic behavior (Movie S1): 1) The actuators gradually converged to the zipped equilibrium ($e = e_{eq}$) and the unzipped equilibrium ($e = 0$) (Fig. 3*A*). In this case, the area of the zipped region of the electrodes increased continuously with time when the actuator contracted (Fig. 3*B* and Movie S2). 2) The actuators transitioned rapidly between the equilibria (Fig. 3*C*). When the voltage turned on, the actuation strain overshot and subsequently exhibited small oscillations around the equilibrium strain (Fig. 3*C*). For these actuators, high-speed videos show that the electrodes "overzipped" and unzipped while the actuation strain overshot (Fig. 3*D* and Movie S3). Subsequently, while the actuation strain oscillated around the equilibrium strain, we did not observe noticeable oscillations of the zipping front (Movie S3). We therefore attribute the oscillations around the equilibrium strain to out-of-plane oscillations of the actuators (Movie S1). As a quantitative measure for the actuation speed, we used the rise time t_R in which the actuators contracted to $e = 0.9e_{eq}$ and the fall time t_F in which the actuators elongated to $e = 0.1e_{eq}$ during the cycle (Fig. 3 *A* and *C*).

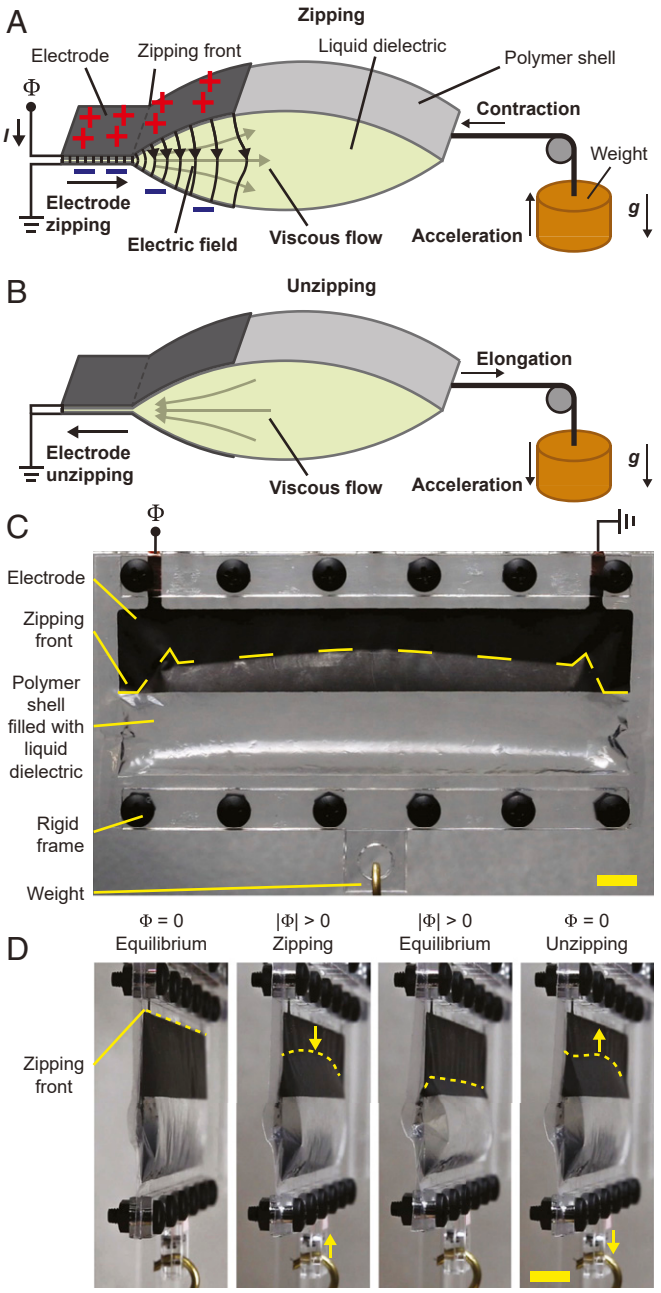

Fig. 1. Dynamics of zipping in electrohydraulic HASEL actuators. (*A*) When a voltage Φ is applied to the actuator, charges flow (*I*) onto its electrodes. The electric field between the charges causes the electrodes to zip together. The liquid dielectric in the shell is displaced against viscous resistance, the actuator contracts, and the attached weight is lifted. (*B*) When the voltage is turned off, the attached weight exerts a tensile force on the shell. The electrodes unzip, and the liquid dielectric flows back between the electrodes against viscous resistance. (*C*) Front view of a zipped Peano-HASEL actuator. (*D*) Skewed view of a Peano-HASEL actuator in different stages of an actuation cycle. (Scale bars, 1 cm.)

Scaling Analysis of the Rise and Fall Times. As the first step of our investigation into the dynamic behavior, we perform a scaling analysis (more details of the analysis may be found in *Scaling analysis* in *SI Appendix*). Fig. 2 *A* and *B* defines all relevant geometrical and material parameters that we use in our analysis.

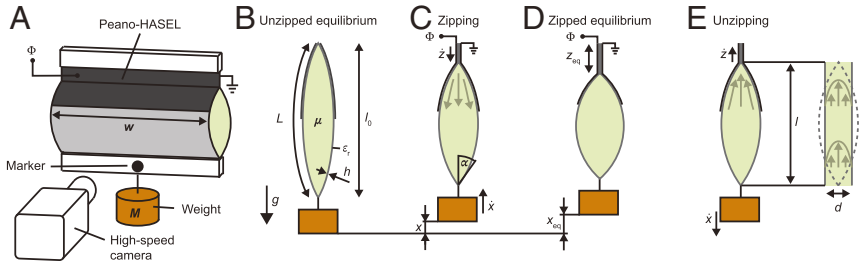

Fig. 2. Experiment to characterize the dynamics of Peano-HASEL actuators. (*A* and *B*) Peano-HASEL actuators were subject to hanging weights *M* and excited with square-wave signals of voltage Φ. The deformation of the actuator as a function of time was measured with a high-speed camera. We investigated the influence of the shell geometry (length *L*; width *w*), the shell material (thickness *h*; relative permittivity ε_r), and the viscosity μ of the liquid dielectric on the dynamic behavior of the actuator. (*C*) When the voltage turns on, the electrodes zip ($\dot{z}$) and the actuator contracts ($\dot{x}$). In the model, we parameterize the shape of the actuator with the angle α. The variable *x* denotes the contraction of the actuator. (*D*) In the zipped equilibrium, the electrodes are zipped over a length z_{eq}, and the actuator is contracted by x_{eq}. (*E*) When the voltage turns off, the electrodes unzip, and the actuator elongates until it returns to the unzipped equilibrium (*B*). In the model, we approximate the fluid flow in the shell as the Poiseuille flow between two parallel plates. Length *l* and spacing *d* of the plates are equal to the length and the average thickness of the liquid-filled region of the pouch, respectively.

At the investigated loads, the elastic strain in the shell is negligible compared to the overall deformation of the actuator. We therefore treat the shell as inextensible. All geometries fulfilled $w > L >> h$, so we can also neglect the bending stiffness of the shells and the mechanical constraints at the sides of the shells (15). In the experiments, we used weights *M* that were at least 10 times larger than the mass of the actuator; therefore, the effects of the mass of the actuator itself on the dynamics were negligible. However, the weights *M* were chosen to be small enough to avoid an instability that causes inhomogeneous zipping of the electrodes under high loads (16). Consequently, the electrodes zipped approximately homogenously from the top edge of the shell, and we approximate the flow of the liquid dielectric as planar. We also neglect the electric field in the unzipped region of the shell, as it rapidly decays away from the zipping front (15–17). The time to charge or discharge the electrodes (~1 μs; see *Estimation of the RC time constant of the actuators* in *SI Appendix*) does not influence the actuator dynamics, as it is much smaller than the observed rise and fall times (t_R, t_F > 1 ms).

Based on the scaling analysis, we introduce a dimensionless voltage:

$$\varphi = \frac{\Phi^2 \varepsilon_0 \varepsilon_r w}{Mgh}, \qquad [1]$$

where ε_0 is the vacuum permittivity and *g* is the gravitational acceleration. This parameter describes the ratio between the electrostatic forces in the zipped region of the electrodes ($\sim\Phi^2\varepsilon_0\varepsilon_r w/h$) and the weight of the load (*Mg*). We have previously shown that this parameter governs the equilibrium strain of Peano-HASEL actuators (15). In the scaling analysis, we look at two limiting cases: $\mu \to 0$ and $\mu \to \infty$. In the limit $\mu \to 0$, viscous effects can be neglected and the inertia of the weight dominates the dynamics. Performing the scaling analysis under this assumption leads to the following:

$$t_n = f_n(\varphi)\left(\frac{L}{g}\right)^{1/2}, \qquad [2]$$

where $f_n(\varphi)$ is an unknown dimensionless function of the dimensionless voltage, and *n* stands for R or F (rise or fall). For a constant value of φ, we therefore expect t_R and t_F to be linearly proportional to the inertial timescale $\tau_i = (L/g)^{1/2}$. In the limit $\mu \to \infty$, viscous effects dominate the dynamic behavior and inertial effects can be neglected. Performing the scaling analysis under this assumption leads to the following:

$$t_n = j_n(\varphi)\frac{\mu w L}{Mg}, \qquad [3]$$

where $j_n(\varphi)$ is an unknown dimensionless function of the dimensionless voltage, and n stands for R or F (rise or fall). In this case, we expect t_R and t_F to be linearly proportional to the viscous timescale $\tau_v = \mu w L/Mg$ when φ is constant.

We confirmed the scaling predicted by Eqs. **2** and **3** experimentally. We measured t_R and t_F for actuators with different geometries and materials systems at different voltages and weights for a wide range of parameters, so that in combination the dimensionless voltage had the constant value $\varphi = 1.13$. When normalized by $\tau_i = (L/g)^{1/2}$ and plotted as a function of the ratio of the two timescales $\tau_v/\tau_i = \mu w L^{1/2}/Mg^{1/2}$, the measured values of t_R and t_F collapsed to single curves (Fig. 4 *A* and *B*). The normalized data show two distinctly different regions. At values $\tau_v/\tau_i \lesssim 4{\cdot}10^{-4}$, the normalized transition times were constant (inertial regime, scaling predicted by Eq. **2**), whereas they were proportional to τ_v/τ_i for values $\tau_v/\tau_i \gtrsim 4{\cdot}10^{-4}$ (viscous regime, scaling predicted by Eq. **3**), confirming the results of the scaling analysis. The two regimes of different scaling behavior also coincide with the two types of observed zipping behavior. 1) In the viscous regime, the actuators gradually converged to the equilibrium strain (Fig. 2*A* and Movie S2). 2) In the inertial regime, the measured actuation strains overshot when the voltage was applied (Fig. 2*C* and Movie S3).

Physical Interpretation of the Inertial and Viscous Timescales. Next, we use simple arguments to derive estimates for the fall time in both regimes in order to explain the origin of the inertial and the viscous timescales and thus to obtain a better understanding of the physics that governs the dynamic behavior of the actuators. In the limit $\mu \to 0$, viscous dissipation due to the liquid dielectric can be neglected. Consequently, the actuator does not resist the fall of the weight after the voltage is turned off. The time in which the mass falls by a distance $x_{eq} = e_{eq}L$ (Fig. 2*D*) in free fall can be calculated as follows:

$$t_{Fi} \approx \left(2e_{eq}\frac{L}{g}\right)^{1/2} \approx 0.24\left(\frac{L}{g}\right)^{1/2}, \qquad [4]$$

where we used $e_{eq}(\varphi = 1.13) \sim 3\%$. This estimate agrees very well with the measured data for $\tau_v/\tau_i \lesssim 4{\cdot}10^{-4}$ (dashed line in Fig. 4*B*). Eq. **4** shows that the inertial timescale $\tau_i = (L/g)^{1/2}$ is a

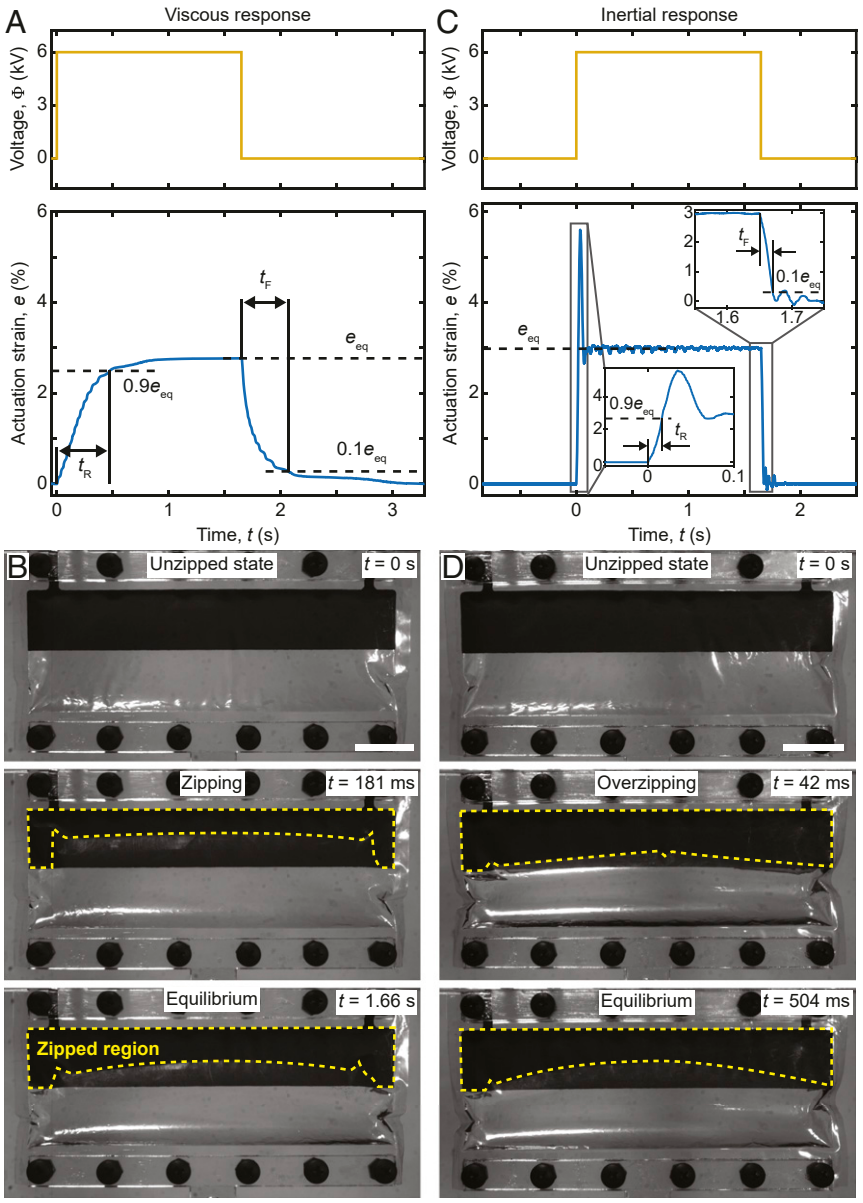

Fig. 3. Viscous and inertial dynamic responses to square-wave voltage signals. (*A* and *B*) Viscous response: actuators converged gradually to the zipped and unzipped equilibria (*A*). In this case, the zipping front moved continuously along the electrode until the actuators reached equilibrium (*B*). (*C* and *D*) Inertial response: the actuators transitioned rapidly between the zipped and unzipped equilibria and the strain overshot during contraction (*C*). In this case, the electrodes "overzipped," and then unzipped for the actuators to reach equilibrium (*D*). As a quantitative measure for the actuation speed, we use the rise time t_R for the actuators to contract to 90% of the equilibrium strain e_{eq} and the fall time t_F for the actuators to elongate to 10% of the equilibrium strain. Geometrical and material parameters of the shells: w = 12 cm, L = 4 cm, h = 20.3 μm, and ε_r = 3.5. Viscosities of the liquid dielectrics: μ = 0.96 Pa·s (viscous response), μ = 4.6 mPa·s (inertial response). Weight and voltage: M = 0.6 kg, Φ = 6 kV. Data shown in *A* and *C* are included in ref. 31. (Scale bars, 2 cm.)

measure for the free-fall time; the numerical prefactor is an estimate for $f_F(\varphi = 1.13)$ in Eq. **2**.

In the limit $\mu \to \infty$, we assume that the weight drops in a quasistatic motion (i.e., the inertia of the weight can be neglected). The weight exerts a tensile force on the actuator, which forces the liquid dielectric to flow back between the electrode against viscous resistance; the actuator acts as a damper that dissipates the potential energy of the weight. The average rate of change of the potential energy is Mgx_{eq}/t_F. Because the aspect ratio of the unzipped region of the shell is large ($l/d \sim 10$, where l and d are its length and average thickness; Fig. 2*E*), we approximate the flow of the liquid dielectric as the Poiseuille flow (32) between two parallel plates of distance d with average flow velocity equal to the average speed z_{eq}/t_F at which the electrodes unzip (z_{eq} is the zipped length of the electrodes in equilibrium; Fig. 2*D*). For the Poiseuille flow, the rate of energy dissipation over a plate section of length l and width w is $12\mu w(z_{eq}/t_F)^2 l/d$. By equating $Mgx_{eq}/t_F \sim 12\mu w z_{eq}^2 l/t_F^2 d$, we obtain an estimate for t_F:

$$t_{Fv} \approx 12\frac{l}{d}\frac{z_{eq}^2}{e_{eq}L}\frac{\mu w}{Mg} \approx 360\frac{\mu w L}{Mg}, \qquad [5]$$

where we used $e_{eq}(\varphi = 1.13) \sim 3\%$ and $z_{eq}(\varphi = 1.13) \sim 0.3L$. This estimate agrees very well with the measured data for $\tau_v/\tau_i \gtrsim 4{\cdot}10^{-4}$ (dotted line in Fig. 4*B*). Eq. **5** shows that the viscous timescale $\tau_v = \mu w L/Mg$ is a measure for the time in which the weight causes the liquid dielectric to flow back between the electrodes

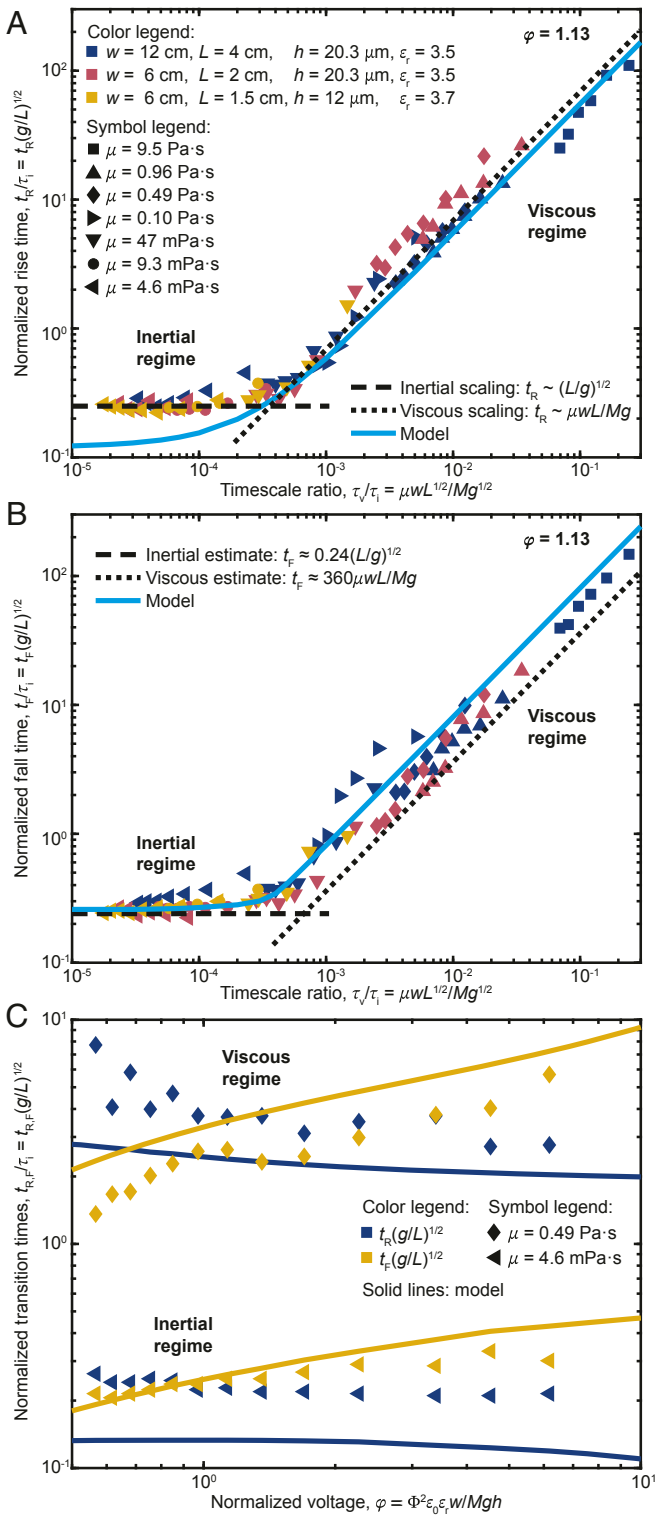

Fig. 4. Measured and calculated rise times t_R and fall times t_F for a wide range of parameters. (*A*) Normalized rise times $t_R/\tau_i = t_R(g/L)^{1/2}$ as function of the timescale ratio $\tau_v/\tau_i = \mu wL^{1/2}/Mg^{1/2}$ measured at the same dimensionless voltage $\varphi = \Phi^2\varepsilon_0\varepsilon_r w/Mgh = 1.13$ for shells of different geometries and materials (marker colors) and liquid dielectrics of different viscosities (marker shapes). All data collapse to a single curve. The curve shows two distinct regimes in which the slope of the curve agrees with inertial scaling (dashed line) and viscous scaling (dotted line), respectively. The blue line is calculated with the model ($\eta = 2.85$). (*B*) Comparison of the corresponding normalized values of the fall times $t_F/\tau_i = t_F(g/L)^{1/2}$ with estimated values in the inertial (dashed line) and viscous (dotted line) regimes and the model (blue line, $\eta = 2.85$). (*C*) Comparison of the measured normalized rise times (blue) and fall times (yellow) as functions of φ for an actuator in the viscous regime (diamonds) and an actuator in the inertial regime (triangles) with model predictions (solid lines, $\eta = 2.85$). Experimental parameters in *C*: $w = 6$ cm, $L = 2$ cm, $h = 20.3$ μm, $\varepsilon_r = 3.5$, and $\Phi = 6$ kV. Data shown in this figure and the code for the numerical model is included in ref. 31.

against viscous resistance; the numerical prefactor is an estimate for $j_F(\varphi = 1.13)$ in Eq. **3**.

Eqs. **4** and **5** also explain the transition between inertial and viscous behavior. When $t_{Fi} > t_{Fv}$, the free-fall time of the weight governs t_F as it is larger than the time for the liquid dielectric to flow back between the electrodes; the actuator lies in the inertial regime (Fig. 4*B*). The transition from inertial to viscous behavior occurs at $t_{Fi} \sim t_{Fv}$ (Fig. 4*B*). When $t_{Fi} < t_{Fv}$, the time for the liquid dielectric to flow back between the electrodes becomes the limiting factor for the actuation speed; the actuator lies in the viscous regime (Fig. 4*B*). For the contraction of the actuator, the same principle holds true. However, in this case, the electrostatic forces drive the deformation.

Numerical Investigation of the Dynamic Behavior. The scaling analysis presented above explains the behavior of the actuators for $\mu \to \infty$ and $\mu \to \infty$, but it is not valid in the transition region between the two regimes, and it cannot predict the transition times for different values of φ without experiments. We use the insights gained from the above estimates to derive a dynamic model for Peano-HASEL actuators to analyze the dependence of t_R and t_F on φ in the inertial and the viscous regimes and in the transition region between the two regimes (see *Dynamic equations of motion* in *SI Appendix* for a step-by-step derivation). In the model, we approximate the shape of the liquid-filled region of the shell with cylinder sections that intersect with an angle 2α (Fig. 2*C*) and treat the liquid dielectric as incompressible (15, 17). Using α as the generalized coordinate, we calculate the equation of motion of the actuator using Lagrange's equations of the second kind (33):

$$\frac{\mathrm{d}}{\mathrm{d}t}\left(\frac{\partial A}{\partial \dot{\alpha}}\right) - \frac{\partial A}{\partial \alpha} = q, \qquad [6]$$

where A is the Lagrangian of the system and q is the generalized force due to viscous dissipation. The Lagrangian can be calculated as follows:

$$A = \frac{1}{2}M\dot{x}^2 - Mgx + \frac{1}{4}\frac{\varepsilon_0\varepsilon_r wz}{h}\Phi^2, \qquad [7]$$

where the first two terms on the right-hand side are the kinetic and potential energies of the weight, and the third term combines the electrical energy of the voltage source and the electrical energy stored in the zipped region of the electrodes. As above, we approximate the fluid flow as the Poiseuille flow between two parallel plates. As the length and the spacing of the plates, we use the length and the average thickness of the liquid-filled region of the shell as a function of α (Fig. 2*E*). As the width of the plates, we use w, and as average flow velocity, we use the zipping speed $\dot{z}$ (Fig. 2 *C* and *E*). These assumptions lead to a generalized dissipative force:

$$q = -24\eta\mu w\frac{\sin(\alpha)^2}{\alpha - 0.5\sin(2\alpha)}\left(\frac{\partial z}{\partial \alpha}\right)^2\dot{\alpha}, \qquad [8]$$

where η is a fitting factor, which accounts for any errors due to the simplification of the fluid flow used for the derivation of q. Combining Eqs. **6**–**8** leads to the equation of motion of the

actuator (the full equation may be found in *Dynamic equations of motion* in *SI Appendix*), which we solved numerically in Matlab to obtain numerical values for t_R and t_F (see code in ref. 31).

At $\varphi = 1.13$, the calculated values of t_F agree well with the experimental results (blue line in Fig. 4*B*) when $\eta = 2.85$. The model also predicts t_R well in the viscous regime (Fig. 4*A*). However, it underestimates t_R in the inertial regime by ~50%. In this regime, applying a voltage excites waves in the liquid dielectric (Movie S3). Exciting those waves requires additional energy. Additionally, the waves lead to inhomogeneous deformation of the shell. Both these effects are neglected in the model; we hypothesize that they explain the deviation of the model from the measured data. To test whether the model can also predict the transition times for other values of φ, we measured them as a function of φ for one actuator in the inertial regime and one actuator in the viscous regime (Fig. 4*C*). In these experiments, the equilibrium strains ranged between ~1% and ~7%. Using the same fitting factor ($\eta = 2.85$), the model consistently overestimates t_F, and underestimates t_R in the viscous regime. A reason for this behavior is the nonlinearity of the viscous flow and the deformation of the shell, which is not fully covered by a single fitting factor (choosing η separately for t_F and t_R gives very good agreement between model and experiment; *SI Appendix*, Fig. S3). In the inertial regime, the model predicts t_F very well, but, like above, t_R is consistently underestimated by ~50%. However, the model correctly predicts the trends of the measured transition times, so it may be used for a qualitative analysis of the dependence of t_R and t_F on φ and τ_v/τ_i in the entire experimentally investigated range.

Fig. 5 shows the values of t_R and t_F normalized by $\tau_i = (L/g)^{1/2}$ as a function of $\tau_v/\tau_i = \mu w L^{1/2}/Mg^{1/2}$ and $\varphi = \Phi^2\varepsilon_0\varepsilon_r w/Mgh$ calculated in the experimentally investigated range of parameters (black squares). The white curves separate the planes spanned by $\Phi^2\varepsilon_0\varepsilon_r w/Mgh$ and $\mu w L^{1/2}/Mg^{1/2}$ into the regions governed by inertia and by viscosity (see *Transition between viscous and inertial regime* in *SI Appendix*). Increasing $\Phi^2\varepsilon_0\varepsilon_r w/Mgh$ increases the electrostatic forces compared to the weight of the attached weights and increases the equilibrium strain (i.e., the distance by which the weight is lifted). In the region dominated by inertia, the net effect is a decrease of t_R with $\Phi^2\varepsilon_0\varepsilon_r w/Mgh$. In contrast, t_F increases with $\Phi^2\varepsilon_0\varepsilon_r w/Mgh$ due to the increased fall distance of the weight. In the region dominated by viscosity, the behavior can be explained by analyzing the shape of the shell. In general, with increasing strain, the viscous resistance due to the liquid decreases because the liquid-filled region of the shell shortens and its average thickness increases (Eq. **8**). Therefore, the value of t_R is predominantly influenced by the viscous resistance at small strains. Increasing $\Phi^2\varepsilon_0\varepsilon_r w/Mgh$ provides a larger electrical force to overcome this initial resistance and thus decreases t_R. The value of t_F is predominantly influenced by the viscous resistance near the zipped equilibrium, which decreases with increasing equilibrium strain. However, t_R only weakly depends on $\Phi^2\varepsilon_0\varepsilon_r w/Mgh$ because the increased fall distance at higher values of $\Phi^2\varepsilon_0\varepsilon_r w/Mgh$ counteracts the decrease in viscous resistance.

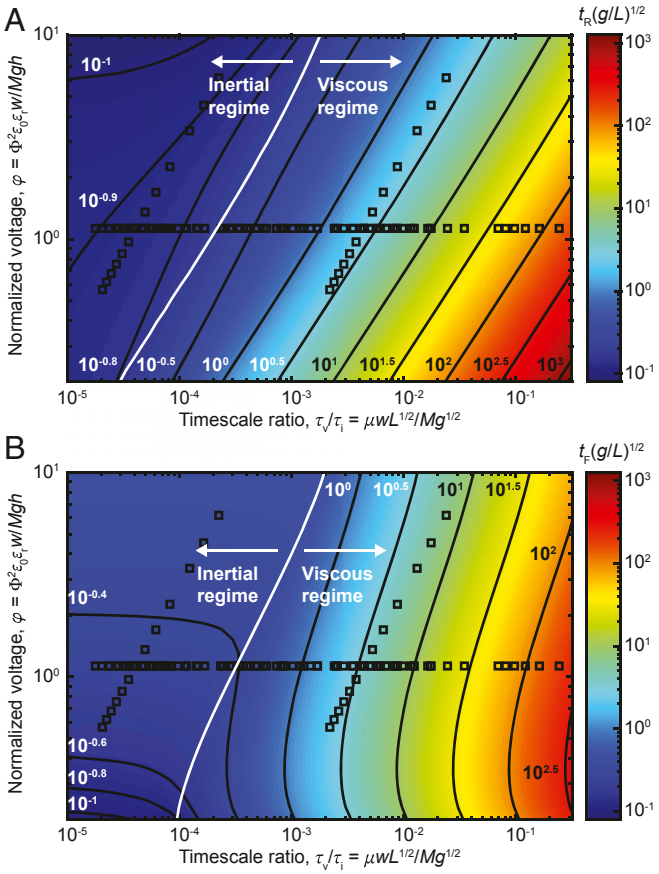

Fig. 5. Calculated rise times t_R and fall times t_F in the range of experimentally investigated parameters. (*A* and *B*) The color contours indicate the normalized rise times (*A*) and the normalized fall times (*B*) calculated with the dynamic model ($\eta = 2.85$) as function of the normalized voltage $\varphi = \Phi^2\varepsilon_0\varepsilon_r w/Mgh$ and the timescale ratio $\tau_v/\tau_i = \mu w L^{1/2}/Mg^{1/2}$. The black squares indicate the experimentally investigated range of parameters. The white curves separate the inertial and the viscous regimes.

Discussion

This paper revealed that there are two dynamic regimes in which the dynamic behavior of Peano-HASEL actuators is entirely different. 1) In the inertial regime, the rise and fall times of the actuators are independent of the viscosity of the liquid dielectric. Consequently, the actuation is governed by the inertia of the attached weight. In this regime, the actuation strain may overshoot before reaching equilibrium and shows an oscillating behavior before equilibrating. In practical applications, the overshoot and the oscillations may be addressed by designing an appropriate control strategy (34). 2) In the viscous regime, viscous resistance of the flow of the liquid dielectric within the shell of the actuator limits the actuation speed. In each regime, we identified a timescale that governs the dynamic behavior. Here, we investigated the rise and fall times of the actuator for rectangular voltage signals that are slow enough for the actuators to equilibrate (i.e., the excitation frequency did not matter). However, the discovered timescales also govern the frequency dependence of the actuation strain for periodic excitation signals, and thus they govern important dynamic characteristics of the actuators, such as resonance and roll-off frequencies (see *Frequency dependence of the actuation strain for a periodic excitation signal* in *SI Appendix*).

Our analysis showed how geometry and materials system of the actuator, and applied load and voltage influence the actuation speed. In particular, Fig. 5 may be used to determine in which dynamic regime Peano-HASEL actuators with specific sets of parameters lie and to estimate their characteristic transition times. For actuators that lie in the viscous regime, the transition times may drastically be reduced by using liquid dielectrics with lower viscosities μ, and by reducing the shell length L ($t_n \sim \mu L$, Eq. **3**) until the actuators enter the inertial regime where the transition times become independent of viscosity; in the inertial regime, the transition times can only be decreased by reducing L ($t_n \sim L^{1/2}$, Eq. **2**). The theoretical model presented in this paper simplified the geometry of the actuators as well as the flow of the liquid dielectric in the shell; it enabled a qualitative analysis of how single parameters influence the dynamics of Peano-HASEL actuators. More accurate theoretical predictions

of the dynamic behavior of Peano-HASEL actuators may be obtained by performing a dynamic multiphysics simulation that simulates the electric field, the deformation of the shell, the flow of the liquid dielectric, and the motion of the mass (e.g., finite-element simulation).

We believe that many types of electrohydraulic soft actuators exhibit an inertial and a viscous dynamic regime. Several types of electrohydraulic actuators exist whose shells consist of thin, inextensible films (12, 35, 36). For these actuators, the presented scaling analysis may readily be modified to identify the governing timescales to account for differences in geometry (12, 35) and modes of electrohydraulic zipping (35, 36). Additionally, the conclusions of this work may be applied to other types of electrohydraulic actuators (12, 13, 37), pumps (38–40), and generators (41) in which elastic deformations play an important role. Elastic strains complicate the theoretical analysis of these transducers, but we also expect them to exhibit an inertial and a viscous regime so that similar strategies can be applied to increase their actuation speed. In general, a reduction of their size may increase the actuation speed of these electrohydraulic transducers; when the viscosity of the working fluid limits the actuation speed, it may be increased substantially by using working fluids with lower viscosity. When designed to operate in the inertial regime, electrohydraulic soft actuators may achieve higher actuation speeds than typically possible with other types of soft actuators. High-speed electrohydraulic soft actuators may enable bio-inspired robots for applications that require fast actuation such as running, jumping, and flying.

Materials and Methods

We fabricated actuators from two types of polymer films: 1) L0WS (Multi-Plastics; thickness $h = 20.3$ μm, relative permittivity $\varepsilon_r = 3.5$) and 2) Mylar 850H/48 (DuPont Teijin Films; $h = 12.0$ μm, $\varepsilon_r = 3.7$). With a CNC heat sealer (12), we bonded the polymer films into rectangular shells of different widths w and lengths L (Fig. 2 *A* and *B*): 1) $w = 12$ cm, $L = 4$ cm; 2) $w = 6$ cm, $L = 2$ cm; and 3) $w = 6$ cm, $L = 1.5$ cm. Then, we screen-printed electrodes (CI-2051; Engineered Materials Systems) onto the top half of both sides of the shells. We filled the shells with silicone oils (viscosities μ ranging from 4.6 mPa·s to 9.5 Pa·s, purchased from Sigma-Aldrich) selecting a volume ($V = wL^2/4\pi$) for which the liquid-filled portion of the shell theoretically forms a cylinder when the electrodes are completely zipped (15). Acrylic frames were attached to the top and the bottom of the shells for load introduction.

In the experiments, we suspended the actuators from the top frame and attached brass weights to the bottom frame (Fig. 2*A*). Rectangular square wave voltages signals of voltage Φ were applied to the actuators with a high-voltage amplifier (Trek Model 50/12; controlled from a computer using LabView). The frequency of the voltage signal was adjusted for each actuator, so it could reach the zipped and unzipped equilibria during a cycle. For each cycle, we reversed the polarity of Φ to reduce charge buildup in the shell (11). We measured the deformation of the actuators by tracking a marker on the bottom frame with a high-speed camera (camera: Vision Research, Phantom v710; tracking software: Tracker).

All data shown in the manuscript and the Matlab code to calculate the transition times are available at Figshare, https://doi.org/10.6084/m9.figshare.c.4965041.v1.

ACKNOWLEDGMENTS. P.R. and C.K. acknowledge support from a Packard Fellowship from The David and Lucile Packard Foundation. S.K. acknowledges support from the University of Colorado Boulder. We acknowledge funding from the Army Research Office (Grant W911NF-18-1-0203), which was used to purchase laboratory equipment to fabricate actuators. We also thank S. Humbert for the use of high-speed camera equipment.

1. C. Majidi, Soft-matter engineering for soft robotics. *Adv. Mater. Technol.* **4**, 1800477 (2018).
2. R. Pelrine, R. Kornbluh, Q. Pei, J. Joseph, High-speed electrically actuated elastomers with strain greater than 100%. *Science* **287**, 836–839 (2000).
3. F. Ilievski, A. D. Mazzeo, R. F. Shepherd, X. Chen, G. M. Whitesides, Soft robotics for chemists. *Angew. Chem. Int. Ed. Engl.* **50**, 1890–1895 (2011).
4. E. Acome *et al*., Hydraulically amplified self-healing electrostatic actuators with muscle-like performance. *Science* **359**, 61–65 (2018).
5. M. T. Tolley *et al*., A resilient, untethered soft robot. *Soft Robot.* **1**, 213–223 (2014).
6. A. Rafsanjani, Y. Zhang, B. Liu, S. M. Rubinstein, K. Bertoldi, Kirigami skins make a simple soft actuator crawl. *Sci. Robot.* **3**, eaar7555 (2018).
7. C. Laschi, B. Mazzolai, M. Cianchetti, Soft robotics: Technologies and systems pushing the boundaries of robot abilities. *Sci. Robot.* **1**, eaah3690 (2016).
8. P. Polygerinos, Z. Wang, K. C. Galloway, R. J. Wood, C. J. Walsh, Soft robotic glove for combined assistance and at-home rehabilitation. *Robot. Auton. Syst.* **73**, 135–143 (2015).
9. P. Polygerinos *et al*., Soft robotics: Review of fluid-driven intrinsically soft devices; manufacturing, sensing, control, and applications in human-robot interaction. *Adv. Eng. Mater.* **19**, 1700016 (2017).
10. F. Carpi, G. Frediani, D. De Rossi, Hydrostatically coupled dielectric elastomer actuators. *IEEE/ASME Trans. Mechatron.* **15**, 308–315 (2010).
11. N. Kellaris, V. Gopaluni Venkata, G. M. Smith, S. K. Mitchell, C. Keplinger, Peano-HASEL actuators: Muscle-mimetic, electrohydraulic transducers that linearly contract on activation. *Sci. Robot.* **3**, eaar3276 (2018).
12. S. K. Mitchell *et al*., An easy-to-implement toolkit to create versatile and high-performance HASEL actuators for untethered soft robots. *Adv. Sci.* **6**, 1900178 (2019).
13. T. Park, K. Kim, S. R. Oh, Y. Cha, Electrohydraulic actuator for a soft gripper. *Soft Robot.* **7**, 68–75 (2020).
14. F. Carpi, G. Frediani, S. Turco, D. De Rossi, Bioinspired tunable lens with muscle-like electroactive elastomers. *Adv. Funct. Mater.* **21**, 4152–4158 (2011).
15. N. Kellaris, V. G. Venkata, P. Rothemund, C. Keplinger, An analytical model for the design of Peano-HASEL actuators with drastically improved performance. *Extreme Mech. Lett.* **29**, 100449 (2019).
16. P. Rothemund, N. Kellaris, C. Keplinger, How inhomogeneous zipping increases the force output of Peano-HASEL actuators. *Extreme Mech. Lett.* **31**, 100542 (2019).
17. G. Moretti, M. Duranti, M. Righi, R. Vertechy, M. Fontana, "Analysis of dielectric fluid transducers" in *Proceedings of SPIE*, Y. Bar-Cohen, Ed. (SPIE, 2018), Vol. 10594, p. 105940W.
18. H. Wang, S. Cai, F. Carpi, Z. Suo, Computational model of hydrostatically coupled dielectric elastomer actuators. *J. Appl. Mech.* **79**, 31008 (2012).
19. T. Lu, S. Cai, H. Wang, Z. Suo, Computational model of deformable lenses actuated by dielectric elastomers. *J. Appl. Phys.* **114**, 104104 (2013).
20. Z. Suo, Theory of dielectric elastomers. *Guti Lixue Xuebao* **23**, 549–578 (2010).
21. C. Keplinger, M. Kaltenbrunner, N. Arnold, S. Bauer, Rontgen's electrode-free elastomer actuators without electromechanical pull-in instability. *Proc. Natl. Acad. Sci. U.S.A.* **107**, 4505–4510 (2010).
22. J. Zhu, S. Cai, Z. Suo, Resonant behavior of a membrane of a dielectric elastomer. *Int. J. Solids Struct.* **47**, 3254–3262 (2010).
23. C. C. Foo, S. Cai, S. J. A. Koh, S. Bauer, Z. Suo, Model of dissipative dielectric elastomers. *J. Appl. Phys.* **111**, 34102 (2012).
24. Y. Chen *et al*., Controlled flight of a microrobot powered by soft artificial muscles. *Nature* **575**, 324–329 (2019).
25. J. Zhu, S. Cai, Z. Suo, Nonlinear oscillation of a dielectric elastomer balloon. *Polym. Int.* **59**, 378–383 (2010).
26. R. Baumgartner *et al*., A lesson from plants: High-speed soft robotic actuators. *Adv. Sci. (Weinh.)* **7**, 1903391 (2020).
27. R. D. Kornbluh, R. Pelrine, Q. Pei, S. Oh, J. Joseph, "Ultrahigh strain response of field-actuated elastomeric polymers" in *Proceedings of SPIE*, Y. Bar-Cohen, Ed. (SPIE, 2000), Vol. 3987, pp. 51–64.
28. B. Mosadegh *et al*., Pneumatic networks for soft robotics that actuate rapidly. *Adv. Funct. Mater.* **24**, 2163–2170 (2014).
29. H. Yuk *et al*., Hydraulic hydrogel actuators and robots optically and sonically camouflaged in water. *Nat. Commun.* **8**, 14230 (2017).
30. B. Gamus, L. Salem, E. Ben-Haim, A. D. Gat, Y. Or, Interaction between inertia, viscosity, and elasticity in soft robotic actuator with fluidic network. *IEEE Trans. Robot.* **34**, 81–90 (2018).
31. P. Rothemund, S. Kirkman, C. Keplinger, Dynamics of electrohydraulic actuators - data and matlab code. Figshare. https://doi.org/10.6084/m9.figshare.c.4965041.v1. Deposited 6 May 2020.
32. D. J. Acheson, *Elementary Fluid Dynamics*, (Clarendon Press, 1990).
33. L. N. Hand, J. D. Finch, *Analytical Mechanics*, (Cambridge University Press, 1998).
34. B. K. Johnson *et al*., Identification and control of a nonlinear soft actuator and sensor system. *IEEE Robot. Autom. Lett.* **5**, 3783–3790 (2020).
35. S. Kim, Y. Cha, Rotary motion and manipulation using electro-hydraulic actuators with asymmetric electrodes. *IEEE Robot. Autom. Lett.* **5**, 3945–3951 (2020).
36. X. Wang, S. K. Mitchell, E. H. Rumley, P. Rothemund, C. Keplinger, High-strain peano-HASEL actuators. *Adv. Funct. Mater.* **30**, 1908821 (2020).
37. I.-D. Sîrbu *et al*., "Electrostatic actuator for tactile display based on hydraulically coupled dielectric fluids and soft structures". *Proceedings of SPIE* **10966**, 109662D (2019).
38. L. Maffli, B. O'Brien, S. Rosset, H. Shea, "Pump it up" in *Proceedings of SPIE*, Y. Bar-Cohen, Ed. (SPIE, 2012), Vol. 8340, p. 83402Q.
39. L. Maffli, S. Rosset, H. R. Shea, Zipping dielectric elastomer actuators: Characterization, design and modeling. *Smart Mater. Struct.* **22**, 104013 (2013).
40. M. T. A. Saif, B. E. Alaca, H. Sehitoglu, Analytical modeling of electrostatic membrane actuator for micro pumps. *J. Microelectromech. Syst.* **8**, 335–345 (1999).
41. M. Duranti, M. Righi, R. Vertechy, M. Fontana, A new class of variable capacitance generators based on the dielectric fluid transducer. *Smart Mater. Struct.* **26**, 115014 (2017).